The Jahn-Teller active fluoroperovskites $A\mathrm{CrF_3}$ $A = \mathrm{Na^+, K^+}$: Magnetic and thermo optical properties

F. L. M. Bernal, F. Lundvall, S. Kumar, P-A. Hansen, D. S. Wragg, and H. Fjellvåg
Centre for Material Science and Nanotechnology, University of Oslo, NO-0315, Norway

O. M. Løvvik
Department of Physics, University of Oslo, NO-0315, Norway and
Sintef Industry, 0314 Oslo, Norway

Chromium (II) fluoroperovskites $A\mathrm{CrF_3}$(A= $\mathrm{Na^+, K^+}$) are strongly correlated Jahn-Teller active materials at low temperatures. In this paper, we examine the role that the A-site ion plays in this family of fluoroperovskites using both experimental methods (XRD, optical absorption spectroscopy and magnetic fields) and DFT simulations. Temperature-dependent optical absorption experiments show that the spin-allowed transitions E_2 and E_3 only merge completely for A= Na at 2 K. Field-dependent optical absorption measurements at 2 K show that the oscillating strength of the spin-allowed transitions in $\mathrm{NaCrF_3}$ increases with increasing applied field. Direct magneto-optical correlations suppress the spin-flip transitions for $\mathrm{KCrF_3}$ below its Néel temperature. In $\mathrm{NaCrF_3}$ the spin-flip transitions vanish abruptly below 9 K revealing magneto-optical correlations possibly linked to crystal structure changes. This suggests that as the long range ordering is reduced local JT effects in the individual $\mathrm{CrF_6^{4-}}$ octahedra take control of the observed behavior. Our results show clear deviation from the pattern found for the isoelectronic $A_x\mathrm{MnF}_{3+x}$ system. The size of the A-site cation is shown to be central in dictating the physical properties and phase transitions in $A\mathrm{CrF_3}$, opening up the possibility of varying the composition to create novel states of matter with tuneable properties.

I. INTRODUCTION

The properties of Jahn-Teller (JT) active materials arise from an intriguing physical interplay between their crystal, orbital and magnetic structures [1]. The hallmark of JT-active systems is orbital frustration (i.e. orbital occupancy degeneracy). This causes structural distortions that break the symmetry and lift the orbital degeneracy [2].

In crystal field theory, the energy levels of an ion with d^n electronic structure in an octahedral field will split into two sets of energy levels: threefold t_{2g} and twofold e_g, separated by an octahedral splitting energy Δ_O. When ions with a d^4 electronic configuration such as $\mathrm{Mn^{3+}}$ are at the center of a $[BX_6^{n-3}]$ octahedron (where B is a cation and X is an anion) there is a further rearrangement of the energy levels, to lower the energy of the highest occupied orbital, creating two tetragonal splitting energies: Δ_e and Δ_t. This is the JT-effect (See Figure 1 (a)). In a system transforming from the octahedral point symmetry O_h to JT distorted D_{4h} (Figure 1 (b)), vibrational modes are introduced corresponding to axial stretching (Q_ϑ) and basal squeezing (Q_ε). The interaction of a doubly degenerate electronic state $E_g(x^2-y^2, 3z^2-r^2)$ with the two e_g modes ($Q_\vartheta, Q_\varepsilon$) is known as the $E \otimes e$ problem (See Ref. [3]). Any point ρ where:

$$\rho = \sqrt{Q_\vartheta^2 + Q_\varepsilon^2} \approx Q_\vartheta \tag{1}$$

in the $(Q_\vartheta, Q_\varepsilon)$ space will correspond to the ground state (since $Q_\vartheta >> Q_\varepsilon$). The energy gained by having a singly occupied rather than doubly degenerate orbital state is known as the JT stabilization energy, E_{JT}, which is proportional to ρ.

The energy level diagram (Figure 1 (b)) shows the point group symmetry (D_{4h}) that develops under JT distortion. There are three possible spin allowed transitions from the ${}^5B_{1g}$ ground state of the D_{4h} point group: $E_1({}^5B_{1g} \rightarrow {}^5A_{1g})$, $E_2({}^5B_{1g} \rightarrow {}^5B_{2g})$ and $E_3({}^5B_{1g} \rightarrow {}^5E_g)$. These spin allowed transitions are defined by the tetragonal splitting parameters and E_{JT} and are related through the octahedral perturbative scheme [3, 4]:

$$E_1 = \Delta_e = 4E_{JT} = K_e Q_\vartheta \tag{2}$$

$E_2 = \Delta_{(eq)}$ and $\Delta_t = E_3 - E_2 = K_t Q_\vartheta$, where K_e and K_t are the electron-ion couplings. It is important to note that all of these phenomena can be explained by the local symmetry of a single octahedron.

Perovskites are crystal structures with the chemical formula ABX_3 based on a network of vertex-sharing octahedral units $[B^{n+}X_6^{m-n}]$, connected through the B-X-B angle (ξ°), the octahedral tilt or perovskite angle. For an ideal cubic perovskite $\xi^\circ = 180^\circ$. In the presence of JT-active ions, the distortions of the octahedra propagate through the crystal lattice, causing ξ° to move away from 180° and favoring the emergence of long range orbital ordering (OO). This has consequences for the magnetic structure of the JT-active perovskite. The ferromagnetic (FM) interactions occur through antiferrodistortive orbital ordering (AOO), e.g. $\left|d_{3x^2-r^2}\right\rangle/\left|d_{3y^2-r^2}\right\rangle$.

X-ray diffraction and optical absorption (OA) spectroscopy experiments under external stimuli (e.g. pressure, temperature, magnetic field) can be used to study

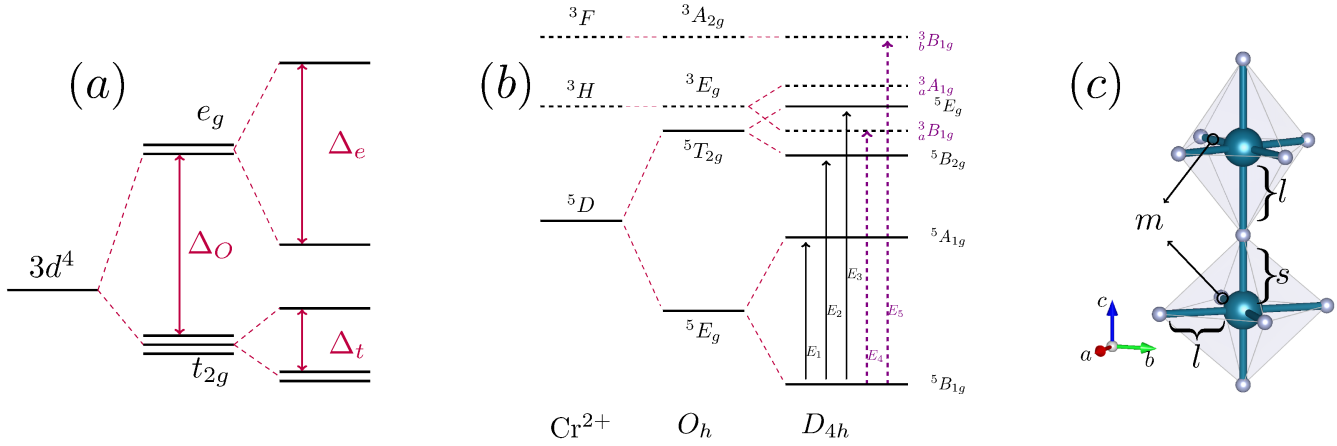

FIG. 1. (a) Evolution of the energy level diagram from the free Cr^{2+} ions into an octahedral crystal field Δ_O followed by its tetragonal JT distortion with two tetragonal splitting parameters Δ_e and Δ_t, and its three spin-allowed transitions. (b) Energy-state diagram under symmetry reduction to D_{4h} owing to the JT-effect, again showing the three spin-allowed transitions E_1, E_2 and E_3, and the spin forbidden transitions E_4 and E_5 (Ref. [9]). (c) A pair of distorted octahedra displaying the short(s), medium (m) and long (l) bonds.

the interplay between the structure and internal degrees of freedom in JT-compounds. Among the most studied JT systems are the ternary alkali metal/manganese (III) low-dimensional fluoroperovskites A'_xMnF_{3+x} (where A' is an alkali/alkali-earth metal and the dimensionality is given by the number of vertex connections between the MnF_6^{3-} octahedra, so the $x = 3, 2, 1$ are 0-,1- and 2-dimensional, respectively). The tetragonal splitting parameters Δ_e and Δ_t of A'_xMnF_{3+x} increase in a linear manner with dimensionality [4]. This manifests itself in the OA spectra as a second set of sharp bands representing the spin-flip transitions. For this family of materials the spin flip bands overlap the spin allowed bands E_1, E_2 and E_3. Valiente et al. and Rodriguez et al suggest that oscillating intensities of the spin-flip bands are correlated to the perovskite angle $\xi°$ [5]. This angle also controls the symmetry allowed overlap between the orbitals of adjacent ions and thus the magnetic exchange interactions. The ocillating strength of the spin-flip bands also depends on the size of the ion at the A-site. The ionic radii of the alkali metals (group 1 of the periodic table) increase significantly with atomic number, providing a good test case for this.

The 2-dimensional fluoride $CsMnF_4$ is a transparent ferromagnet which adopts the tetragonal space group $P4/n$ at room temperature [6]. The magneto-structural properties of $CsMnF_4$ at high pressure have been thoroughly studied. High pressure synchrotron X-ray diffraction (SXRD) experiments showed that $CsMnF_4$ goes through a tetragonal-to-orthorhombic phase transition from $Pa/n \rightarrow Pmab$ at about $\sim$1.6 GPa [7]. Magnetic susceptibility measurements show that this is accompanied by a ferromagnetic to antiferromagnetic (FM-to-AFM) phase transition. OA spectroscopy reveals a high-to-low spin transition at 37.5 GPa in which the three spin-allowed transition bands merge into one [5]. The explanation for this is that as the pressure increases E_{JT} is surpassed by the octahedral crystal field splitting energy, Δ_O, forcing Mn^{3+}into the octahedral low spin configuration. This high-to-low spin transition is not observed for the smaller A' -site atoms, Na^+ and K^+[7–9].

Chromium (II) fluoroperovskites have been difficult to study owing to the oxygen-sensitive chemistry of Cr^{2+} ions. $KCrF_3$ (which can be prepared by a solid state route) has three temperature dependent polymorphs: cubic ($T > 1000$ K), tetragonal ($T = 1000$ to 250 K) and monoclinic ($T < 250$ K); where the tetragonal to cubic phase transition is suggested to correspond to a metal-insulator transition (MIT) as the OO is removed and orbitals become degenerate[10, 11]. The role of OO in driving the high-temperature structural transition in $KCrF_3$ has also been studied theoretically (See Ref. [12] and literature therein). There are in addition three magnetic phases (incommensurate-AFM (IC-AFM) between 300 and 79.5 K (T_N), commensurate-AFM (C-AFM) between T_N and 45 K, weak FM and canted AFM below 10 K) [13].

We recently developed a synthesis route for $NaCrF_3$ and were able to explore its structural and magnetic properties for the first time [14]. It has a triclinic structure ($P\bar{1}$) at 300 K with a single canted-AFM magnetic structure below 21 K[14]. Measurements of field dependent magnetization ($M(H)$) below the Néel temperature have revealed the onset of a metamagnetic transition at an applied field of 8 T.

In this paper we study the importance of the A-site ion size in the three dimensional perovskite family $ACrF_3$ where $A = Na^+$ (small) or K^+ (large) using temperature

and field-dependent OA spectroscopy, supported by crystal structure analysis and DFT calculations. In general we see that as the symmetry of the system is reduced the long range magnetic interactions become weaker and local magnetic structures begin to dominate the behaviour. Our results show that the changes in the spin-flip transitions at low temperature are not correlated to the perovskite angle ξ°, but rather to the magnetic exchange interactions between neighboring CrF_6^{4-} octahedra. Merging of the spin-allowed spectral bands E_2 and E_3 for $A = Na^+$ shows the emergence at low temperature of an intermediate electronic state where Δ_t is zero. Furthermore, when an increasing external magnetic field is applied at 2 K, the intensity of the spin allowed bands increases for $NaCrF_3$ but not for $KCrF_3$.

E_{JT} is larger in $NaCrF_3$ compared to $KCrF_3$, owing to the smaller size of the Na^+ ion. Again, we believe this is explained by the local orbital and magnetic ordering rather than the perovskite angle ξ°. We also present density functional theory (DFT) simulations which calculate the superexchange parameters for the different magnetic orderings possible in each crystal structure, and so, determine the OO of each phase. Finally, we show that the synthesis method we described for $NaCrF_3$ [14] can also be used to produce large volumes of high purity $KCrF_3$.

II. METHODS

$NaCrF_3$ was prepared according to the method described by Bernal et al. [14] $KCrF_3$ was prepared by a similar method: 0.5 g of chromium (II) acetate hydrate ($Cr_2(CH_3CO_2)_4(H_2O)_2$; CrOAc) was dissolved in 2 ml deagassed water in a polycarbonate vial sealed with a silicone rubbber septum under constant flow of Ar. In a second sealed polycarbonate vial 0.3 g KHF_2 was dissolved in 10 mL degassed water. The KHF_2 solution was then injected with a dry syringe into the CrOAc solution. $KCrF_3$ precipitated immediately. Washing with pure methanol rendered both samples air stable. The washed samples were dried under vacuum overnight, and then stored in a glove-box.

Powder XRD measurements for $KCrF_3$ were performed at the Norwegian Resource Centre for X-ray Diffraction, Scattering and Imaging (RECX) on a Bruker D8 Advance diffractometer in capillary mode with $Cu_{k\alpha}$ radiation selected by a Cu (111) focusing monochromator and a LynxEye XE detector. Synchrotron powder XRD data for $NaCrF_3$ were collected at the Swiss-Norwegian Beam line (SNBL) BM01A of the European Synchrotron (ESRF), Grenoble, France. The setup is described elsewhere [15]. The diffuse reflectance spectra (DRS) were collected on polycrystalline samples of $NaCrF_3$ and $KCrF_3$ with a UV-3600 photospectrometer (Shimadzu). The low temperature OA experiments were conducted under vacuum in a closed cycle cryostat (Janis Research) with a Fibre-Lite MI-150 halogen lamp (Dolan-Jenner Industries) and USB4000 spectrometer (OceanOptics) in the temperature range 11 - 300 K, and from 1.3 to 2.7 eV.

Field dependent magnetization measurements were carried out on the AC magnetic measurement system -II (ACMS-II) using a vibrating sample magnetometer (VSM) on the Quantum Design (QD) Physical Property measurement system (PPMS). Samples of known weight were loaded into weakly diamagnetic plastic holders and immobilized on brass sample holders at defined height of approximately 25 mm from the bottom of the brass holder. This holder was then loaded into the ACMS-II at the end of a long plastic rod and inserted into the PPMS and cooled down to 2 K. Sample was kept at 2 K for 30 minutes before starting magnetization measurements for thermal homogenization of the sample. The magnetization measurements were carried in sweep mode from 0 to +/- 9 T at a ramp rate of 0.01 T/second and a measurement was taken each second.

Magneto-optic measurements were carried out in a Quantum Design PPMS system. A custom insert was developed using an external DH-2000 Halogen lamp (Mikropack) and USB4000 spectrometer (OceanOptics), both optically connected with the insert using an optical fibre. A long silica rod with the sample powder attached in a gelatin capsule at one end was used to bring light in and out of the vacuum sample chamber and to position the sample appropriately with respect to the PPMS's superconducting magnets. A LakeShore Cryotronics CERNOX thermometer was utilized for reading local sample temperature close to the sample.

For temperature dependent measurements, the silica rod mounted sample was inserted into the PPMS cavity and the entire space was evacuated to a soft vacuum at room temperature. The sample and cavity were thermally stabilized before the cool down process was initiated. Cool down from 300 to 2 K was carried out at the rate of 0.5 K/ min and an optical spectrum was taken every 10 seconds. Once the system reached the 2 K temperature set-point a 30 minute delay was given in order for the sample temperature to stabilize, all the while continuously measuring the OA spectra. Magnetic field dependent OA measurements, were made at 2 K and the magnetic field was ramped at 0.01 T/second up to 9 T, continuously measuring OA.

The electronic structures of the $NaCrF_3$ (triclinic- $\mathcal{I}$) and $KCrF_3$ (monoclinic- $\mathcal{M}$, tetragonal- $\mathcal{T}$, and cubic- $\mathcal{C}$) phases were calculated using the Vienna *ab initio* simulation package (VASP)[16, 17] with the PBE general gradient approximation (GGA) [18]. $KCrF_3$- $\mathcal{C}$ was included for comparison, as the highest possible symmetry. The cutoff energy of the plane wave basis set expansion was at least 450 eV. The density of the k point density was determined by a maximum distance between points of 0.25 $Å^{-1}$. Hubbard-corrected GGA+U calculations were performed according to the method described by Meredig *et al.* [19] with the Coulomb interaction parameter U going up to $U = 9$ eV and the exchange interaction parameter $J_H = 0.88$ for chromium 2+. For the calculation of the

superexchange parameters, we used the same parameters as in the GGA+U calculations on four possible configurations:

- **F**, (ferromagnetic) in which all the spins are parallel;
- **A**, (antiferromagnetic) in which the intralayer spins are parallel while the interlayer spins are antiparallel;
- **C**, in which the chains of spins along the z-axis are ferromagnetically coupled, while adjacent chains are aligned antiparallel;
- **G**, in which all nearest neighbor spins are antiparallel.

III. RESULTS

A. Structural Analysis of $A\mathrm{CrF_3}$

To analyze the $A\mathrm{CrF_3}$ systems, we use a pseudocubic lattice (PL) derived from the unit cell of the high T cubic $\mathrm{KCrF_3}$ phase. Its vertices lie at the centers of 8 neighboring $\mathrm{CrF_6^{4-}}$ octahedra, and its lattice parameters are $a_p{\approx}b_p{\approx}c_p$. The JT distorted octahedra have short (s, ca. 1.9 $\AA$), medium (m, ca. 2.0 $\AA$) and long (l, ca. 2.3 $\AA$) Cr-F bonds, the relative orientation of which depends on the orbital ordering. The s, m and l bonds can be used to describe the orientations of isolated $\mathrm{CrF_6^{4-}}$ octahedra. For example, the tilt angle ξ_l° along the l-bonds can be described as l-axial, and if a bond lies within the plane formed by the s and m bonds, then it is described as the sm-plane of the octahedra. The octahedral distortion parameter Δd used to quantify the distortion is also calculated from the s, m and l Cr-F bond lengths around the octahedron:

$$\Delta d = 1/6 \sum_{i=1}^{6} |\mathrm{l}_i - \mathrm{l}_{av}|/\mathrm{l}_{av} \quad (3)$$

Where l_i for i = 1-6 is the 6 Cr-F bond lengths, (2 each of s, m and l) and l_{av} is the average of s, m and l [20].

In general we can describe all of the structures as having layers in the s, l plane where neighboring octahedra are rotated 90° about the m-axis to create a motif of alternating s and l Cr-F bonds. These layers are linked by m Cr-F bonds. The PL is aligned relative to the tetragonal ($\mathcal{T}$), monoclinic ($\mathcal{M}$) and triclinic ($\mathcal{I}$) crystallographic unit cells such that the network of alternating s and l bonds lies in the a_p, b_p plane and the linking m bonds are aligned along c_p (see Figure 2 (c)). Figure 2 (c) shows the relationship of the PL to the ($\mathcal{T}$), ($\mathcal{M}$) and ($\mathcal{I}$) unit cells of the $A\mathrm{CrF_3}$ family. The tilts (ξ°) of the octahedra relative to the edges of the ideal PL increase as the symmetry is lowered. The layers of alternating s and l bonds in the a_p, b_p plane are stacked with adjacent layers mirrored in the a_p, c_p plane. This creates an A, B, A, B... sequence. At the orbital level this means that the OO consists of $\left|d_{3x^2-r^2}\right\rangle/\left|d_{3y^2-r^2}\right\rangle$ AOO layers stacked along the c_p-axis.

TABLE I. Octahedral tilt angles $\xi^\circ(\mathcal{I})$ and distortions (Δd) from XRD for $A\mathrm{CrF_3}$. $\xi^\circ(\mathcal{I})$ for $\mathrm{NaCrF_3}$ and $\xi^\circ(\mathcal{M})$ for $\mathcal{M}$-$\mathrm{KCrF_3}$ are taken from [13]. $\xi^\circ(\mathcal{T})$ is fixed to 180° (ξ^π) by symmetry. The calculated octahedral distortions Δd ($\times 10^{-4}$)are given for all phases.

Cr	$\Delta d^{\mathcal{T}}$	$\Delta d^{\mathcal{M}}$	$\Delta d^{\mathcal{I}}$	
1:	65.70	56.53	78.85	
2:	-	69.97	55.86	
3:	-	-	76.24	
4:	-	-	70.73	
		$\xi^\circ(\mathcal{M})$		
Cr1-F3-Cr2 :			180.0	l-axial
Cr1-F2-Cr2 :			164.3	sm-planar
Cr1-F1-Cr2 :			162.3	sm-planar
		$\xi^\circ(\mathcal{I})$		
Cr1-F5-Cr3 :			138.797	l-axial
Cr2-F2-Cr1 :			139.446	sm-planar
Cr2-F1-Cr1 :			146.589	sm-planar
Cr4-F6-Cr2 :			140.526	l-axial
Cr4-F4-Cr3 :			142.357	sm-planar
Cr4-F3-Cr3 :			141.683	sm-planar

In an ideal cubic perovskite all $\xi^\circ = 180$ (ξ^π). The higher the number of ξ^π vertex-angles in a system, the stronger the magnetic exchange interactions due to proper orbital overlap. To the ideal system described by the PL, we applied the perturbative model [3, 4] to describe the structural parameters related to the JT-distortions from the XRD-patterns. Inspection of the powder XRD pattern (Figure 2) confirmed that our syntheses yielded single phase polycrystalline $\mathcal{T}$-$\mathrm{KCrF_3}$ (space group $I4/mcm$) and $\mathcal{I}$-$\mathrm{NaCrF_3}$ (space group $P\bar{1}$) at room temperature. Octahedral distortion parameters Δd for the three $A\mathrm{CrF_3}$ phases, and perovskite tilt angles ξ° for $\mathcal{M}$-$\mathrm{KCrF_3}$ and $\mathcal{I}$-$\mathrm{NaCrF_3}$ are given in Table I.

Δd for $\mathcal{T}$-$\mathrm{KCrF_3}$ is $65.7{\times}10^{-4}$. It adopts the zero-tilt configuration described by Glazer notation $a^\circ a^\circ a^\circ$ [21] so

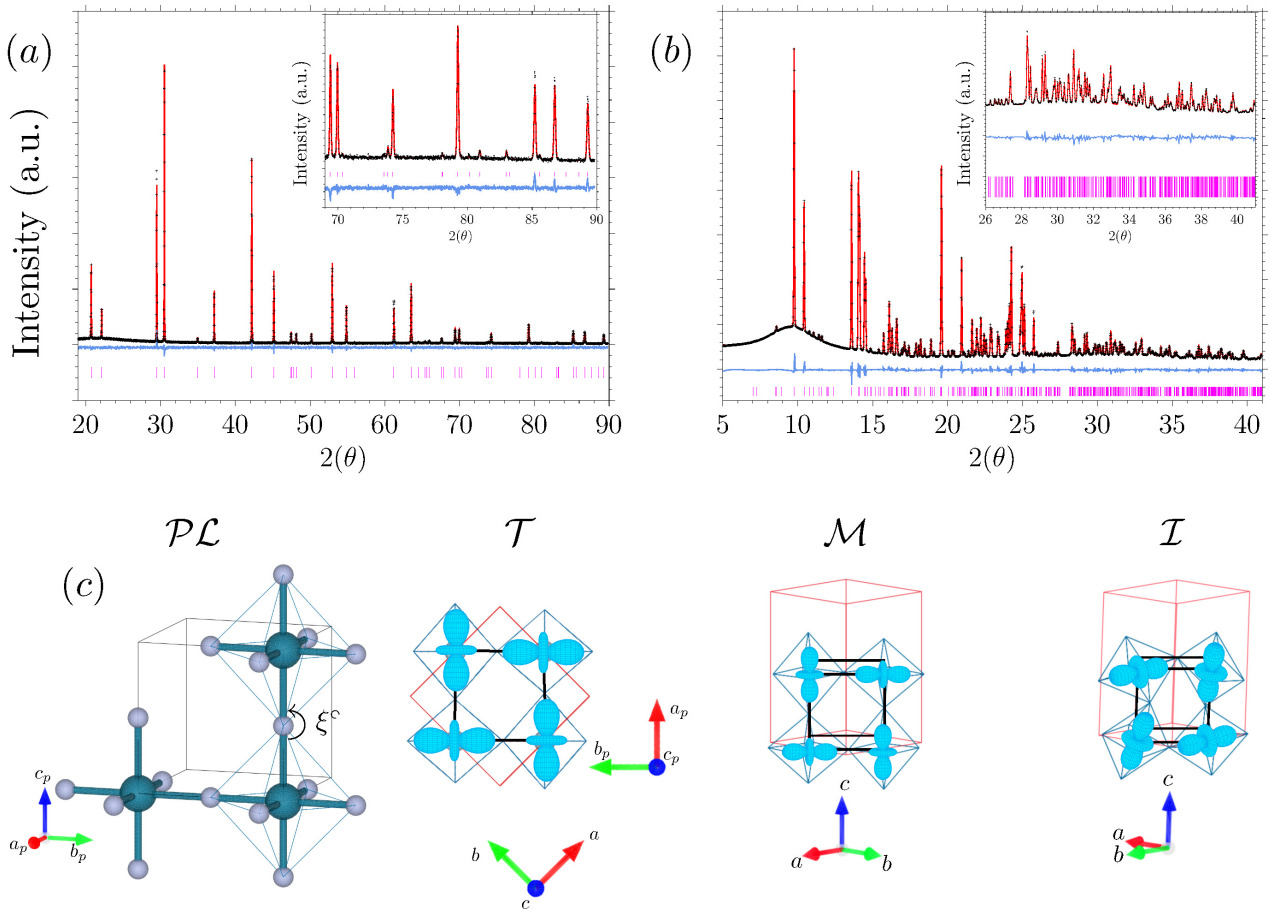

FIG. 2. (a) Observed (black dots) and calculated (red line) X-ray powder diffraction (XRD) for T-KCrF$_3$ ($\lambda = 1.5405$ Å) at 258 K ($a = 6.051317$, $c = 8.024635$ Å). Agreement factors of the Rietveld refinement: $R_{wp} = 16.09476$ %; $R_{exp} = 5.3272$ %. The solid blue line shows the difference between the observed and calculated intensities, and the ticks indicate the allowed Bragg reflection positions. The inset shows the high angle fit. (b) Final observed Synchrotron XRD profiles ($\lambda = 0.709$ Å of NaCrF$_3$ at 298 K ($a = 5.5100$, $b = 5.69190$, and $c = 8.18860$ Å). The agreement of the Rietveld refinement: $R_{wp} = 3.321219$ and $R_{exp} = 0.014351$ %. The very low R_{wp} value is due to the use of an area detector [22]. (c) Schematic representations of, from left to right: the pseudocubic unit cell with $a_p = b_p = c_p$ ($\mathcal{PL}$), the PL embedded within the tetragonal ($\mathcal{T}$), monoclinic ($\mathcal{M}$) and triclinic ($\mathcal{I}$) unit cells of ACrF$_3$. The OO motif of the $|d_{3i^2-r^2}\rangle$ ($i = x, y, z$) orbitals is shown.

that all periovskite angles are ξ^π. The ξ^π angles within the AOO layers create strong in-plane FM interactions propagating along the a_p and b_p axes. The magnetic superexchange parameters within the AOO-planes display FM character through σ interactions between half-filled $|d_{3z^2-r^2}\rangle$ and empty $|d_{x^2-y^2}\rangle$ Cr^{2+} orbitals bridged by $|p_\sigma\rangle$ orbitals of F$^-$ ions. The orthogonal ξ^π perovskite angle along the c_p-axis (absent in the low dimensional A'_xMnF$_{3+x}$ systems) leads to a ferrodistortive OO (FOO) with an AFM coupling between adjacent overlapping empty $|d_{x^2-z^2}\rangle$ and $|d_{y^2-z^2}\rangle$ orbitals bridged by F$^-|p_\sigma\rangle$ orbitals.

$\mathcal{M}$-KCrF$_3$ (space group $I112/m$) appears on cooling to T =250 K [10]. Two crystallographically non-equivalent Cr sites (Cr1, Cr2) are generated in this form with Δd values of 56.53×10^{-4} and 69.97×10^{-4}. Within the a_p, b_p and b_p, c_p planes there are tilts corresponding to Glazer notation $a^-b^-c^0$, in which, the Cr1-F1-Cr2 and Cr1-F2-Cr2 angles are 162 and 167°, respectively. The loss of symmetry leaves a single ξ^π vertex angle along the c_p-axis where proper orbital overlap is preserved for FM interactions to propagate. The orbital overlap for AFM interactions along the c_p axis becomes weaker, reflecting on weak FM interactions since the $|d_{x^2-z^2}\rangle - |p_\sigma\rangle - |d_{y^2-z^2}\rangle$ bridge is weakened.

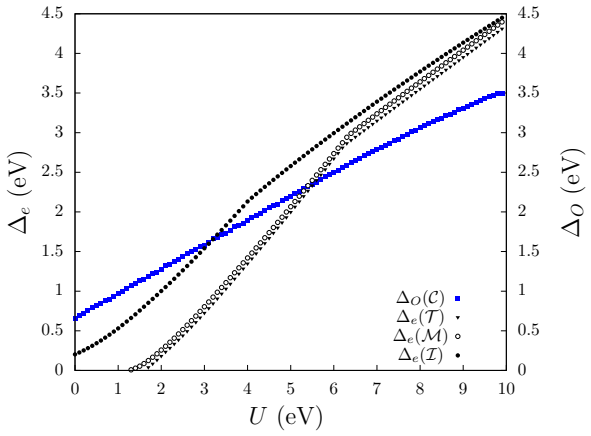

FIG. 3. Calculated octahedral Δ_O and tetragonal Δ_e splitting parameters as function of U. $\Delta_O(\mathcal{C})$ octahedral splitting of the cubic phase of KCrF$_3$, tetragonal $\Delta_e(\mathcal{T})$ for the tetragonal phase, $\Delta_e(\mathcal{M})$ for the monoclinic phase and $\Delta_e(\mathcal{I})$ corresponding to the triclinic space group in NaCrF$_3$.

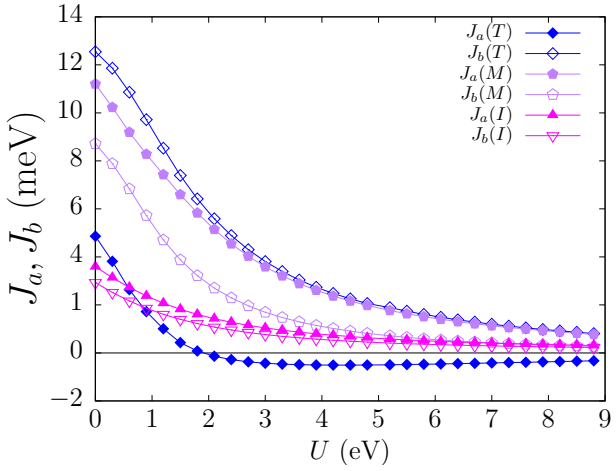

FIG. 4. Calculated axial J_A and basal J_B magnetic exchange parameters for $\mathcal{T}$-KCrF$_3$($I4/mcm$), $\mathcal{M}$-KCrF$_3$($I112/m$) and $\mathcal{I}$-NaCrF$_3$($P\bar{1}$)-phases as function of U. Ferromagnetic exchange for $J_i > 0$ and antiferromagnetic for $J_i < 0$.

NaCrF$_3$ crystallizes in a NaCuF$_3$ type structure with space group $P\bar{1}$ [23]. Four nonequivalent crystallographic sites (i.e. Cr1, Cr2, Cr3 and Cr4) are present for Cr^{2+} in NaCrF$_3$ [14], with Δd and ξ° values given in Table I. The Δd values for NaCrF$_3$ are greater than those of the KCrF$_3$ phases, indicating greater JT distortion. The CrF_6^{4-} units are tilted in all directions, adopting the Glazer tilt $a^-b^-c^-$. This means that NaCrF$_3$ has no ξ^π angles, which is reflected in a significant reduction in the strength of the overall magnetic interactions. Consequently, the AOO adopts a canted motif where $|d_{3z^2-r^2}\rangle$ orbitals on Cr1 and Cr4 tilt about the b_p-axis and Cr2 and Cr3 are tilted about the a_p-axis.

B. Electronic Structure of ACrF$_3$

The calculated octahedral and tetragonal splitting parameters for the ACrF$_3$ phases, as a function of the electron-electron correlation parameter U, are presented in Figure 3. For $\mathcal{C}$-KCrF$_3$ there is no JT distortion and the octahedral splitting parameter Δ_O is present at all levels of correlations, preserving the orbital degeneracy of the e_g orbitals.

This invariance under U suggests that electron-electron correlations lead to neither OO nor MIT in $\mathcal{C}$-KCrF$_3$ within the framework of our calculations. For $\mathcal{T}$- and $\mathcal{M}$-KCrF$_3$ phases, the emergence of the tetragonal splitting parameter Δ_e occurs simultaneously at $U \approx 1.7$ eV. This may suggest that the OO and MIT in both $\mathcal{T}$- and $\mathcal{M}$-KCrF$_3$ phases emerge as a consequence of strong electron correlations. However, the calculations were performed on the already distorted low symmetry KCrF$_3$ which excludes electron-electron correlations as the source of the OO. In other words, structural distortion is necessary for OO to occur. Replacing K^+ with Na^+ in ACrF$_3$ increases $E_{JT} = \Delta_e/4$ even at $U = 0$ and from this point its increase with U has a similar curvature to $\mathcal{T}$- and $\mathcal{M}$-KCrF$_3$. Our calculations support the structural results where E_{JT}, which is related to Q_ϑ (Equation 2), is larger for NaCrF$_3$ than KCrF$_3$. At $U = 0$ NaCrF$_3$ preserves the orbital degeneracy of the e_g orbitals showing that the phonon-electron interactions that characterise the JT-effect are the driving force for OO.

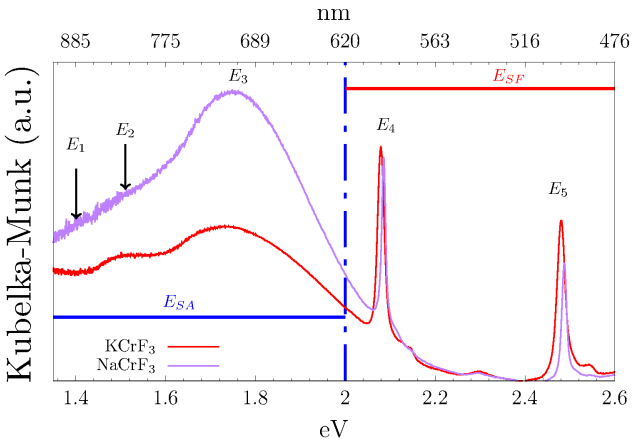

FIG. 5. OA spectra of KCrF$_3$ and NaCrF$_3$ at 300 K. Spin-allowed (quintet-quintet) E_{SA} transitions: E_1, E_2 and E_3. Spin-flip (quintet-triplet) E_{SF} transitions: E_4 and E_5.

We calculated the ground-state energies of the low-symmetry ACrF$_3$ phases with four magnetic orderings $\mathbf{A}, \mathbf{F}, \mathbf{C}, \mathbf{G}$ and then the magnetic exchange parameters J_B (basal) within the a_pb_p-plane of the pseudocu-

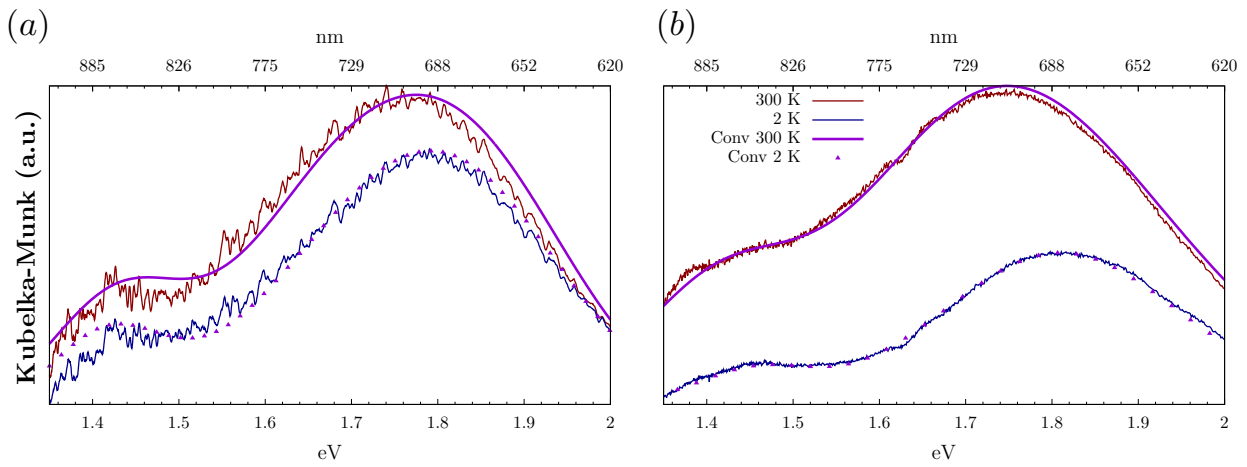

FIG. 6. OA spectra of (a) KCrF$_3$ and (b) NaCrF$_3$ at 300 and 2 K corresponding to the E_{SA} region with their respective convolution fits.

TABLE II. Calculated JT vibrational modes and fitted spin-allowed band positions in the OA spectra of ACrF$_3$. The normal modes are calculated from the bond distances in the octahedral units in Å according to Equations 4. Fitted positions of the E_{SA}^{300K} bands in eV at 300 K. Tetragonal parameters $E_1 = \Delta_e$ and $\Delta_t = E_3 - E_2$ along with the JT-stabilization energy E_{JT} given in eV.

Cr	$Q_\vartheta(\mathcal{T})$	$Q_\vartheta(\mathcal{M})$	$Q_\vartheta(\mathcal{I})$	$Q_\varepsilon(\mathcal{T})$	$Q_\varepsilon(\mathcal{M})$	$Q_\varepsilon(\mathcal{I})$
1:	0.33	0.30	0.43	0.019	0.071	0.042
2:	-	0.38	0.32	-	0.024	0.068
3:	-	-	0.40	-	-	0.034
4:	-	-	0.42	-	-	0.036

E_{SA}^{300K}	E_1	E_2	E_3	Δ_t	E_{JT}
KCrF$_3$	1.42	1.65	1.82	0.20	0.355
NaCrF$_3$	1.40	1.66	1.78	0.12	0.350

E_{SA}^{2K}	E_1	E_2	E_3	Δ_t	E_{JT}
KCrF$_3$	1.42	1.65	1.82	0.20	0.355
NaCrF$_3$	1.45	1.76	1.79	0.025	0.362

bic unit cell, and J_A (axial) along the c_p-axis according to: $J_A = [E(\mathbf{F}) - E(\mathbf{G}) - E(\mathbf{A}) + E(\mathbf{C})]/4S^2$ and $J_B = [E(\mathbf{F}) - E(\mathbf{G}) + E(\mathbf{A}) - E(\mathbf{C})]/8S^2$ [24]. Figure 4 shows the energies of the superexchange parameters as function of U for the tetragonal, monoclinic and triclinic phases of ACrF$_3$. For $\mathcal{T}$-KCrF$_3$ the calculated axial superexchange parameter is $J_A(\mathcal{T}) > 0$ for $U < 1.9$, and become weakly negative for $U \geq 2$ suggesting weak AFM interactions between AOO layers. The basal superexchange $J_B(\mathcal{T})$ decreases at all levels of correlations but is always positive with $J_B(\mathcal{T}) > J_A(\mathcal{T})$. This picture agrees with the one described in the structural section, in which $\mathcal{T}$-KCrF$_3$ contains only ξ^π vertex angles, both within its AOO a_p, b_p-plane (with strong in-plane FM interactions) and connecting the AOO layers. In $\mathcal{M}$-KCrF$_3$, the loss of symmetry leaves a single ξ^π along the c_p-axis. The calculated superexchange parameters of $\mathcal{M}$-KCrF$_3$ confirm that $J_A(\mathcal{M}), J_B(\mathcal{M}) > 0$ with $J_A(\mathcal{M}) > J_B(\mathcal{M})$, the opposite of the tetragonal form. Again, this agrees with the structural analysis, describing a single ξ^π in the c_p-axis direction, giving strong FM interactions propagated along the c_p-axis.

In NaCrF$_3$, the smaller Na$^+$ ion on the A-site induces additional octahedral tilts in all directions with no ξ^π vertex angles, accompanied with larger octahedral distortions (Table I). This further reduces strength of the magnetic interactions as the orbital overlap decreases. The canted AOO propagates within the $a_p c_p$-plane. NaCrF$_3$ has $J_A(\mathcal{I}) \sim J_B(\mathcal{I}) > 0$ with increasing U. Comparing to the higher symmetry systems found in KCrF$_3$, $J_{A(B)}(\mathcal{M}) > J_{A(B)}(\mathcal{I})$ indicates that the magnetic interactions are weakest at the lowest symmetry. We observe that $J_A(\mathcal{T}) > J_{A,B}(\mathcal{M}) > J_{A,B}(\mathcal{I})$ for $U < 4$ but for $U \geq 4$ $J_A(\mathcal{T})$ and $J_A(\mathcal{M})$ converge. Again this is consistent with the structural analysis, where increasing distortion reduces orbital overlap.

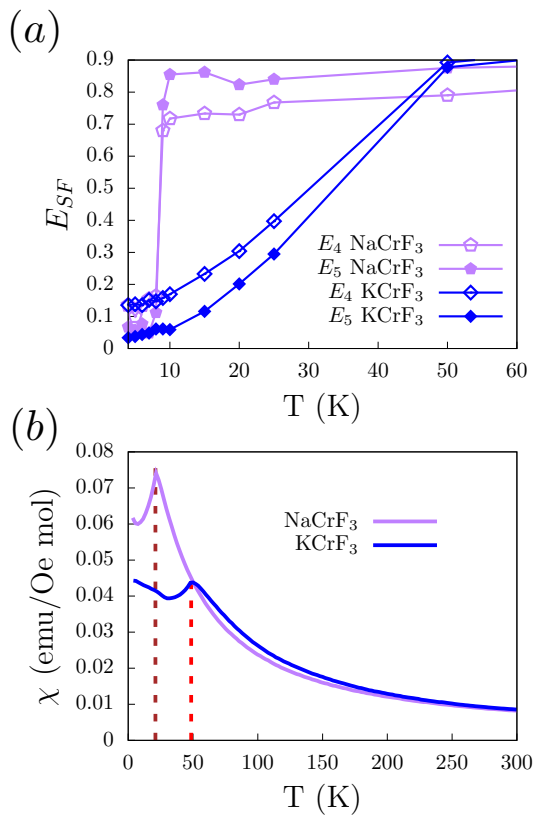

FIG. 7. (*a*) Temperature dependent OA of E_{SF} transitions E_4 and E_5 for $KCrF_3$ and $NaCrF_3$ and (*b*) ZFC magnetic susceptibility χ in the interval 2 to 300 K. The two vertical dashed lines at $T_N = 21.5$ K (brown) and $T_1 = 48.6$ K (red) indicate the Néel temperature of $NaCrF_3$ and the IC-to-AFM transition in $KCrF_3$, respectively.

C. Temperature and magnetic field dependent OA Spectroscopy

Figure 5 shows the OA-spectra at 300 K for $KCrF_3$ and $NaCrF_3$, respectively. The spectra are very similar in the location of the observed bands. For $ACrF_3$ there is no overlap between the spin allowed and the spin forbidden transitions, in contrast to the A_xMnF_{3+x} family. The quintet-quintet or spin-allowed (E_{SA}) transitions (Figure 1 (*b*) and (*c*)) lie between 1.3 and 2 eV. They are labeled here as E_{SA} corresponding to $E_1(^5B_{1g} \rightarrow {}^5A_{1g})$, $E_2(^5B_{1g} \rightarrow {}^5B_{2g})$ and $E_3(^5B_{1g} \rightarrow {}^5E_g)$. The region between 2 and 2.6 eV contains the quintet-triplet, or spin-flip (E_{SF}) transitions: $E_4(^5B_{1g} \rightarrow {}^3_aB_{1g})$ and $E_5(^5B_{1g} \rightarrow {}^3_bB_{1g})$. The E_{SF} bands for both phases have similar oscillating strengths despite $NaCrF_3$ having no ξ^π vertex angles.

We conducted temperature dependent OA measurements in the PPMS between 300 and 2 K and fitted the E_{SA} bands with a convolution of three Gaussian functions, $\alpha t^2 e^{(-\beta(E-E_i)^2)}$ (Figure 6 (*a*) and (*b*), respectively). Inspection of the temperature-dependent OA measurements conducted in the PPMS confirms the patterns observed in the preliminary experiments shown in Figure 5. The fitted positions and oscillating intensities of the spin allowed bands at 300 K and 2 K are given in Table II along with the Δ_t and E_{JT} values. The E_{SA} transitions of $KCrF_3$ are $E_1 = 1.42$, $E_2 = 1.65$ and $E_3 = 1.82$ eV at 300 K. At 2 K the positions of E_1, E_2 and E_3 remain almost the same but their intensities decrease. The JT-stabilization energy E_{JT} (Equation 2) for $KCrF_3$ is 0.355 eV at 300 K and remains nearly unchanged down to 2 K. The second tetragonal parameter, Δ_t, is 0.20 eV at 300 K and also remains unchanged down to 2 K. The E_{SA} energy transitions of $NaCrF_3$ are $E_1 = 1.40$, $E_2 = 1.66$, and $E_3 = 1.785$ eV at 300 K. At 2 K E_1 and E_2 shift to higher energies by 50 meV and 448 meV, respectively. This means that reduction of ion size at *A*-site induces an increment in E_{JT} of 12.5 meV at 2 K which in turn is 7.5 meV higher than E_{JT} of $KCrF_3$. The fit at 2 K shows that there is a total merging of the E_2 and E_3 bands as shown in Figure 6 (*b*). It follows that the tetragonal parameter Δ_t of $NaCrF_3$ disappears and that $\Delta_e/\Delta_t \rightarrow \infty$ as $\Delta_t \rightarrow 0$. This means that with decreasing temperature contributions to E_{JT} from σ bonding become stronger in $NaCrF_3$ than $KCrF_3$. This effect is due to the reduced symmetry caused by the ion size reduction at the *A*-site. The vibrational mode frequencies Q_ϑ and Q_ε for $ACrF_3$ are calculated from the bond lengths by:

$$Q_\vartheta = (1/\sqrt{3})(2l - m - s), \quad Q_\varepsilon = m - s \qquad (4)$$

The values are given in Table II. For all three phases $Q_\vartheta >> Q_\varepsilon$ which suggests that orbitals with $|d_{3z^2-r^2}\rangle$ symmetries are being occupied. The normal tetragonal mode Q_ϑ (i.e. stretching of octahedral unit) increases on average with decreasing symmetry. Since $E_{JT} \sim Q_\vartheta \sim \rho$ (See Equation 1) we see that $Q_\vartheta(\mathcal{I}) > Q_\vartheta(\mathcal{M}) > Q_\vartheta(\mathcal{T})$ in Table II thus the E_{JT} for $NaCrF_3$ is larger than in $KCrF_3$ indicating that the reduction of the *A*-ion size reinforces the JT-phenomenon.

We integrated the intensities of the two E_{SF} bands for all temperatures. Figure 7 (*a*) shows the fitted E_{SF} intensities in both phases as a function of temperature, and Figure 7 (*b*) shows the zero-field cooling (ZFC) magnetic susceptibility, χ, of both phases at an applied magnetic field of 1 T. The temperature (T_1) in $KCrF_3$ corresponding to the IC-AFM to C-AFM transition (Ref. [13]) and the Néel temperature (T_N) of $NaCrF_3$ are 48.6 K and 21.5 K respectively, with both having magnetic moments $\mu_{eff} \sim 4.47\mu_B$ following the spin-only configuration $S = 2$ for Cr^{2+}. The two samples obey the Curie-Weiss (CW) law in different temperature ranges: 300-100 K for $KCrF_3$ and 300-24 K for $NaCrF_3$. The Curie temperatures θ of $KCrF_3$ and $NaCrF_3$ are 1.7 and -4 K respectively (Refs. [13],[14]). We observe that the normalized integrated intensities E_{SF} of $KCrF_3$ start decreasing smoothly at its C-AFM magnetic ordering at T_1. This is not observed for the case of $NaCrF_3$ where the

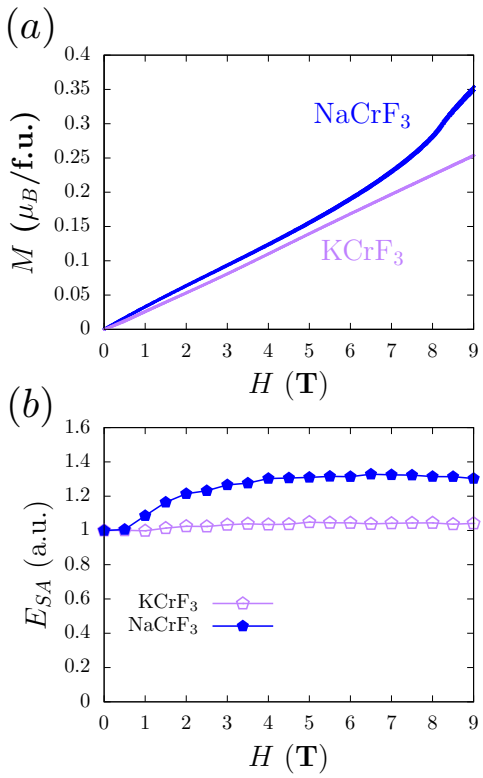

FIG. 8. (a) Isothermal half-loop magnetization curves for an applied magnetic field ($M(H)$) from 0 to 9 T and then back to 0 at 2 K for $KCrF_3$ and $NaCrF_3$. (b) Magnetic field dependent OA of E_{SA} transitions (in the range 650-750 nm, equivalent to E_3) for $KCrF_3$ and $NaCrF_3$ at 2 K between 0-9 T, normalized to the absorption at zero field.

E_{SF} intensities decrease abruptly between 9 and 8 K and not at the C-AFM point at 21.5 K. The disappearance of the E_{SF} bands is likely to lead to a thermochromic effect, but we have not as yet been able to observe this.

After the temperature reached 2 K, we performed field dependent OA experiments for both $KCrF_3$ and $NaCrF_3$ to explore possible correlations with field dependent experiments in which metamagnetic transitions were observed for $NaCrF_3$ (Ref. [14]). Quick inspection of the measurements in Figure 8 (a) shows that the plot for $KCrF_3$ is linear while that of $NaCrF_3$ is not. This agrees with our previous results [14]. Notice however that the presence of metamagnetism in $NaCrF_3$ and its absence in $KCrF_3$ occurs in the range of investigated fields. Further high-field experiments could elucidate better understanding of this particular magnetic behavior. Figure 8 (b) shows the integrated intensities of the E_{SA} bands E_2 and E_3 of $KCrF_3$ and $NaCrF_3$ as a function of magnetic field in steps of 0.5 T in the field region between 0 - 9 T at 2 K. The integrated normalized oscillating strength of the E_{SA} transitions in $NaCrF_3$ increases with magnetic field, while for $KCrF_3$, it remains constant. We didn't observe significant variations in the intensities of the E_{SF} peaks under magnetic field.

IV. DISCUSSION

The JT-active $ACrF_3$ systems, where, $A = K^+, Na^+$ display interesting magneto-optic and structural phenomena under external stimuli. XRD reveals that with decreasing ion size at the A-site, E_{JT} increases as $Q_\vartheta(\mathcal{I}) > Q_\vartheta(\mathcal{T}) > Q_\vartheta(\mathcal{M})$.

Calculations of the JT splitting parameters for all phases of $ACrF_3$ show that: (1) the electron-ion JT $E\otimes e$ coupling is essential for the OO to occur. (2) A MIT was observed for $\mathcal{T}$ and $\mathcal{M}$ for $U > 1.5$ eV. This indicates that for OO to occur, JT-distortions must already be in place. This is confirmed with the substitution $K^+ \rightarrow Na^+$ since in $NaCrF_3$ at zero electron-electron correlation the tetragonal splitting parameter Δ_e is zero (ie., $\Delta_e \neq 0$ for all U). Since the stabilization energy $E_{JT} = \Delta_e/4$, a direct correlation between the results of the structural analysis and the calculations supports that $E_{JT}(\mathcal{I}) > E_{JT}(\mathcal{T}, \mathcal{M})$.

As symmetry is lowered and the number of ξ^π decreases, so does the strength of the magnetic interactions. This establishes a magneto-structural correlation between the ξ° vertex angles and the magnetic superexchange parameters. The calculated superexchange parameters J_A and J_B show that by decreasing the lattice symmetry (and thereby the number of ξ^π vertex angles) the magnetic interactions reduce in strength regardless of U. Note that the formulas used for the calculation of the superexchange parameters are only valid for the high symmetry phases with orthogonal angles. A generalized mathematical description is required to include deviations from the orthogonal angles.

Thanks to the fact that the E_{SA} and E_{SF} bands in the OA spectra of $ACrF_3$ do not overlap, we can address the effect of external stimuli on the two types of transition independently.

Temperature dependent OA-measurements show that for $KCrF_3$ the E_{SA} transitions are not effected by temperature in the range studied. For $NaCrF_3$ the E_{SA} transitions are shifted to higher energies with decreasing temperature with E_2 and E_3 actually merging at 2 K. This means that Δ_t tends to becomes zero, which indicates that electron-ion couplings arising from π-couplings in $NaCrF_3$ are nearly absent and $\Delta_e/\Delta_t \rightarrow \infty$.

The E_1 band in $NaCrF_3$ shows a slight blue-shifting at 2 K, which can be interpreted as an increase in E_{JT} with respect to $KCrF_3$, again showing that reducing the size of the ion at the A-site increases E_{JT}. The Δ_e values obtained from the OA-measurements of $ACrF_3$ lie between Δ_e values of A'_3MnF_6 and A'_2MnF_5 [4]. Δ_e, and thus E_{JT} for $ACrF_3$ do not follow the linear relation between Δ_e and dimensionality proposed for the A_xMnF_{3+x} family.

The E_{SF} bands of both systems vanished with decreasing temperature. This behavior has previously been observed on the 2D ferromagnetic K_2CrCl_4 and Rb_2CrCl_4

[25, 26]. Magnetic field dependent OA-spectra measurements in Rb_2CrCl_4 show a decline in intensity of the energy transitions with increasing magnetic field [26]. We did not observe significant changes in the E_{SF} bands under increasing magnetic field in $A\mathrm{CrF_3}$. The increase in E_{SA} band intensity with increasing magnetic field for $\mathrm{NaCrF_3}$ at 2 K is not observed for $\mathrm{KCrF_3}$ and the above mentioned systems.

The increase could be related to the orbital structure and spin ordering correlations described in the Kugel-Khomskii Hamiltonian [27]. However, at this point we cannot establish a direct correlation between the two effects and further theoretical and experimental studies are necessary for proper interpretation of these results.

No significant changes in the E_{SF} intensities are observed in the OA-spectra of $\mathrm{KCrF_3}$ at the $\mathcal{T}$-to-$\mathcal{M}$ transition. Based on the $A_x\mathrm{MnF}_{3+x}$ family, in which the E_{SF} transitions are related to ξ° and thus to the magnetic superexchange interactions $J_{A(B)}$, we expected the intensities to decrease as the number of ξ^π is reduced. Instead of changing at the crystallographic phase transition, the E_{SF} intensities of $\mathrm{KCrF_3}$ drop at the IC-to C-AFM transition at $T_1 = 48.6$ K.

In $\mathrm{NaCrF_3}$ the E_{SF} transition intensities decrease abruptly below 9 K instead of at the Néel temperature of 21.5 K as might be expected. The magnetic susceptibility measurements of $\mathrm{NaCrF_3}$ show a weak ferromagnetic upswing between 9 and 8 K which coincides with the fall in the E_{SF} intensities. The reduction of the E_{SF} at T_1 in $\mathrm{KCrF_3}$ and at 9 K in $\mathrm{NaCrF_3}$ indicates that the intensity of E_{SF} is controlled by the magnetic structure and not the crystal structure, a direct magneto-optical correlation. No magneto-structural correlations were observed at standard pressure in either temperature or field dependent OA experiments.

V. CONCLUSIONS

The magneto-optical and structural properties of fluoroperovskites $A\mathrm{CrF_3}$ where $A = \mathrm{Na^+, K^+}$ display trends that contrast strongly with those reported for the $A_x\mathrm{MnF}_{3+x}$ family.

Analysis of the E_{SA} bands in the OA spectra (supported by DFT calculations and XRD characterization) shows that having the smaller $\mathrm{Na^+}$ ion at the A-site increases the JT- stabilization energy, E_{JT}. Field-dependent OA measurements of the E_{SA} in $\mathrm{NaCrF_3}$ show magneto-optical correlations absent in $\mathrm{KCrF_3}$ and other related structures. The collapse of the E_{SF} intensities in $A\mathrm{CrF_3}$ below 48.6 K is directly linked to the local magnetic interactions and not the crystal structure the more the order of the structure is reduced, the more significant the local interactions based on the magnetic properties of individual $\mathrm{CrF_6^{4-}}$ octahedra become. In conclusion, the ion size at the A-site controls the physical properties of the $A\mathrm{CrF_3}$ fluoroperovskites. This, combined with the reliable synthesis routes we have developed for this family of materials, opens up the possibility of discovering novel states of matter by manipulating the A-site.

VI. ACKNOWLEDGEMENTS

The authors would like to thank Prof. Serena Margadonna (University of Swansea, Swansea, UK) for granted financial support from the Norwegian Research Council (Norges Forskningsråd NFR) through project 214260. We acknowledge use of the Norwegian national infrastructure for X-ray diffraction and scattering (NFR project number 208896). The computational calculations were performed on resources provided by UNINETT Sigma2 - the National Infrastructure for High Performance Computing and Data Storage in Norway through grant No. nn2615k.

[1] Z. Nussinov and J. van den Brink. *Rev. Mod. Phys*, **87**, 1, 2015.
[2] H. A. Jahn and E. Teller. *P. Roy. Soc A-Math Phy*, **161**, 220, 1937.
[3] R. Valiente, F. Rodríguez. *Phys. Rev. B*, **60**, 9423, 1999.
[4] F. Rodríguez, F. Aguado. *J. Chem. Phys.*, **118**, 10867, 2003.
[5] F. Aguado, F. Rodríguez, and P. Nunez. *Phys. Rev. B*, **76**, 094417, 2007.
[6] W. Massa, and M. Steiner. *J. Solid State Chem.*, **32**, 137, 1980.
[7] M. C. Moron, F. Palacio, S. M. Clark, A. Paduan-Filho. *Phys. Rev. B*, **51**, 8660, 1995.
[8] M. C. Morón, F. Palacio and J. Rodríguez-Carvajal. *J. Phys. Matter*, **5**, 4909, 1993.
[9] F. Aguado, F. Rodríguez, and P. Nunez. *Phys. Rev. B*, **67**, 205101, 2003.
[10] S. Margadonna and G. Karotsis. *J. Amer. Chem. Soc.*, **128**, 16436, 2006.
[11] S. Margadonna and G. Karotsis. *J. Mater. Chem.*, **17**, 2013, 2007.
[12] C. Autieri, E. Koch, and E. Pavarini. *Phys. Rev. B*, **89**, 155109, 2014.
[13] Y. Xiao, Y. Su, H. F. Li, C. M. N. Kumar, R. Mittal, J. Persson, A. Senyshyn, K. Gross, and Th. Brueckel. *Phys. Rev. B*, **82**, 094437, 2010.
[14] F. L. M. Bernal, J. Sottmann, Ø.S. Fjellvåg, C. Drathen, W. A. Sławinski, O. M. Løvvik, D. S. Wragg and H. Fjellvåg *Phys. Rev. Materials*, **4**, 054412, 2020.
[15] V. Dyadkin, P. Pattison, V. Dimitriev and D. Chernyshov *J. Synchrotron Rad.*, **23**, 825, 2016.
[16] G. Kresse, J. Furthmüller. *Phys. Rev. B*, **54**, 11169, 1996.
[17] G. Kresse, J. Hafner. *Phys. Rev. B*, **47**, 558, 1993.
[18] J. P. Perdew, K. Burke, and M. Ernzerhof. *Phys. Rev. Lett*, **77**, 3865, 1996.

[19] B. Meredig, A. Thompson, H. A. Hansen, C. Wolverton, and A. van de Walle. *Phys. Rev. B*, **82**, 195128, 2010.
[20] W.H. Baur. *Acta Crystallogr., Sect. B: Struct. Sci.*, **30**, 1195, 1974.
[21] A. M. Glazer *Acta Cryst.*, **B28**, 3384, 1972.
[22] W. I. F. David *J. Res. Natl. Inst. Stand. Technol.*, **109**, 107, 2004.
[23] V. Keiser, M. Otto, F. Binder, and D. Babel. *Z. Anorg. Allg. Chem.*, **585**, 93, 1990.
[24] G. Wang, Z. Li, L. Zheng, and Z. Yang. *Phys. Rev. B*, **84**, 045111, 2011.
[25] P. Day, A.K. Gregson, and D.H. Leech. *Phys. Rev. Lett.*, **30**, 19, 1973.
[26] E. Janke, T.E. Wood, C. Ironside and P. Day. *J. Phys, C: Solid State Phys.*, **15**, 3809, 1982.
[27] K. I. Kugel and D. I. Khomskii *Sov. Phys. Usp*, **25**, 231, 1982.